
CHALMERS
UNIVERSITY OF TECHNOLOGY

# Pulsed HEMT LNA Operation for Qubit Readout



Citation for the original published paper (version of record):
Zeng, Y., Stenarson, J., Sobis, P. et al (2025). Pulsed HEMT LNA Operation for Qubit Readout. IEEE Transactions on Microwave Theory and Techniques, In Press.
http://dx.doi.org/10.1109/TMTT.2025.3556982



(article starts on next page)

# Pulsed HEMT LNA Operation for Qubit Readout

Yin Zeng, *Graduate Student Member, IEEE*, Jörgen Stenarson, *Member, IEEE*, Peter Sobis, and Jan Grahn, *Senior Member, IEEE*

***Abstract*—Large-scale qubit readout in quantum computing systems requires highly sensitive amplification with minimal power consumption to reduce the thermal load and preserve qubit integrity. We propose a pulse-operated cryogenic low-noise amplifier (LNA) scheme that minimizes the influence of the LNA on qubit operation and reduces power consumption by duty cycling. A modified commercially available cryogenic hybrid LNA based on InP high-electron mobility transistors (HEMTs) has been characterized to demonstrate the feasibility of pulsed operation for qubit readout. The transient noise and gain performance of the LNA were obtained through a cryogenic time domain noise measurement setup with 5-ns time resolution and a measured noise standard deviation (SD) below 0.3 K. The time-domain noise and gain performance of the LNA in response to a square gate voltage waveform were investigated. Through an analysis of the LNA's recovery limitations, we developed a fast recovery bias strategy leading to the optimization of the gate voltage waveform using a genetic algorithm (GA). This resulted in a strong enhancement of transient noise and gain performance with a recovery time of 35 ns. The drain current transients were measured to calculate the average power consumption of the pulse-operated LNA, which confirmed a reduction in average power consumption proportional to the duty cycle. This work contributes to the development of high-performance and low-power amplifier solutions critical for large-scale qubit readout applications.**

***Index Terms*—Cryogenic, InP high-electron mobility transistor (HEMT), low power, low-noise amplifier (LNA), pulsed operation, qubit readout.**

## I. Introduction

SUPERCONDUCTING quantum computers show great promise for solving complex problems beyond the capabilities of classical computers [1]. Nowadays, noisy mid-size superconducting quantum computers have already outperformed traditional supercomputers in computationally demanding problems, such as random circuit sampling [2], [3], [4]. Following the road map to massively scale up physical qubits and enable efficient error correction, superconducting quantum computers are on track to unlock their full potential [5], [6], [7], [8].

Received 9 December 2024; revised 27 February 2025; accepted 27 March 2025. This work was supported by the Advanced Digitalization Program under WiTECH Centre CRYTER through VINNOVA, Low Noise Factory AB, Virgina Diodes Inc., AAC Omnisys, and RISE Research Institutes of Sweden. *(Corresponding author: Yin Zeng.)*

Yin Zeng and Jan Grahn are with the Department of Microtechnology and Nanoscience (MC2), Chalmers University of Technology, 412 96 Göteborg, Sweden (e-mail: yzeng@chalmers.se; jan.grahn@chalmers.se).

Jörgen Stenarson and Peter Sobis are with Low Noise Factory AB, 412 63 Göteborg, Sweden (e-mail: stenarson@lownoisefactory.com; sobis@lownoisefactory.com).

Digital Object Identifier 10.1109/TMTT.2025.3556982

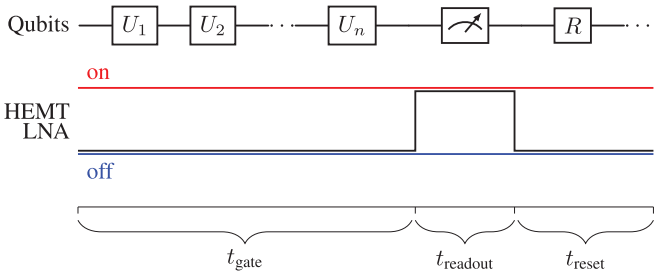


Fig. 1. Timing diagram for qubit operation with a pulsed HEMT LNA readout scheme. The top row depicts the qubit manipulation sequence, where $U_1$–$U_n$ represent arbitrary gate pulses, followed by a readout pulse represented by the meter symbol and a qubit reset phase $R$. The middle row illustrates the HEMT LNA "ON" and "OFF" states during the sequence. The bottom row indicates the timing of the gate operation $t_{\text{gate}}$, readout $t_{\text{readout}}$, and reset $t_{\text{reset}}$ phases.

A critical component at the 4-K stage in current quantum systems is the InP high-electron mobility transistor (HEMT) low-noise amplifier (LNA), which serves as the second-stage amplifier for qubit readout after parametric amplification at the mK stage. The HEMT LNA plays an essential role in qubit readout by simultaneously amplifying around ten frequency-multiplexed signals with power levels around −120 dBm, while introducing minimal added noise [9], [10]. With the upscaling of quantum systems, the number of HEMT LNAs will increase, meaning a challenge in overall thermal budget. Since amplifier back action—referring to the undesired influence from the amplifier on the qubit environment inducing higher energy state transitions and readout errors—has been reported to excite two-level systems [11], [12], a higher total dc power from the HEMT LNAs may also pose a problem for qubit integrity [13]. Consequently, bulky and lossy isolators and circulators have to be used, which may hinder the scalability of qubit architectures [11].

One approach to mitigate the backaction noise is by enhancing the isolation of the first stage parametric amplifier. Reported techniques include canceling the reciprocity through frequency convention [14] or integrating the parametric amplifier with on-chip peripheral circuitry [15]. In addition, due to the pulsed readout nature of qubits, the implementation of superconducting switches with parametric amplifiers to enable time-sequential operation was explored [16]. However, several of these amplifier solutions suffer from limited bandwidth or require complex setups involving additional parametric processes [17].

Recent studies have been conducted to reduce the dc power consumption of the HEMT LNA through optimization of the

InP HEMTs combined with advanced semiconductor modeling and low-power microwave circuit design [18], [19], [20], [21]. While these methods push the limits of current device technology and microwave design, they often come at the cost of noise and gain performance including bandwidth. Achieving lower dc power consumption in the HEMT without compromising its key merits has become more challenging.

To address these limitations, we propose in this work to implement pulsed HEMT LNA operation for qubit readout. This will leverage the pulse-readout nature of qubits, as illustrated in Fig. 1. The HEMT LNA is activated only during the qubit readout pulse and turned off otherwise. This strategy reduces average power consumption through duty cycle while maintaining the amplifier's gain and noise performance during the critical readout windows. By synchronizing the amplifier's operation with the qubit readout pulse, this approach may also minimize the amplifier backaction interference with qubit gate operations and reduce the thermal population of the qubit readout resonator when idling.

Nonetheless, implementing pulsed operation for the HEMT LNA in qubit readout introduces demanding requirements for the LNA's transient noise and gain response, which remains largely uncharacterized. The qubit readout pulse duration, which must be significantly shorter than the qubit's decoherence time to ensure high-fidelity measurements, typically ranging from tens of nanoseconds to several microseconds depending on the design of the readout circuits [22], [23], [24], [25], [26], [27]. In some demanding qubit readout scenarios, such as surface code error correction protocols combined with reset, ancilla qubits are read out at microsecond-level intervals, with readout durations of several hundreds of nanoseconds [7], [8], [27], [28], [29]. Hence, it is crucial that the HEMT LNA minimizes its deadtime—the period where the amplifier dissipates power but its noise and gain are not yet stable enough to enable readout—to fully exploit pulsed operation and potentially achieve a 5–10 times reduction in average power consumption [8], [27], [28], [29].

This work addresses the noise and gain of the cryogenic HEMT LNA in the time domain and proposes an optimized pulsed operation scheme suitable for qubit readout. We first assess the static performance of a cryogenic HEMT LNA modified for pulsed operation followed by the development of a calibrated cryogenic transient noise and gain measurement setup with 5-ns resolution and noise standard deviation (SD) below 0.3 K. This setup allowed us to measure the LNA's transient response under pulsed square-waveform gate bias. To address the recovery limitations, we developed a fast recovery bias strategy, optimizing the gate voltage waveform using a genetic algorithm (GA) to ensure rapid recovery with minimal noise. Our results show that the pulse-operated scheme reduces power consumption proportional to the duty cycle thus confirming the feasibility of the proposed approach. This article contributes to smarter LNA operation by demonstrating the first transient noise measurement of a cryogenic HEMT LNA, showing that state-of-the-art noise performance can be maintained in a pulsed bias mode. This advancement is crucial for reducing power dissipation and minimizing qubit disturbance, both being key factors for scalable quantum computing.

## II. Device Under Test

The device under test (DUT) in this work was a modified LNF-LNC4-8C [30], a commercially available InP HEMT LNA abundant in quantum systems [3], [9], [26]. The schematic of the DUT before and after modification is shown in Fig. 2(a). The DUT consists of one dc bias PCB and four RF PCBs. To enable faster transient operation, modifications were made to the low-pass filter on the gate bias on the dc bias PCB. The 10-kΩ series resistor was replaced with a short, and the 1-kΩ parallel resistor was removed. In addition, the 100-nF capacitor was changed to 1 nF. The real circuit before modification and a zoomed-in-view of the modified dc PCB are shown in Fig. 2(b) and (c), respectively.

The static noise and gain of the DUT under cryogenic conditions were characterized with an Agilent N8975B NFA using the cryogenic attenuator $Y$-factor method, as illustrated in Fig. 2(d) [31]. The DUT was biased with a drain voltage of $V_D = 0.7$ V and a drain current of $I_D = 15$ mA, corresponding to a dc power consumption of $P_{\mathrm{dc}} = 10.5$ mW. The measured average gain and noise temperature of the DUT at 4 K were 44.4 dB and 1.2 K, respectively, representing the typical performance when the LNA is used for superconducting qubit readout amplification. Since the transient performance measurement was conducted at a temperature of 10.6 K, the static gain and noise at 10.6 K were measured as a reference, which was 44.4 dB and 1.8 K, respectively. The change in ambient temperature mainly affected the noise temperature whereas gain remained stable for both temperatures.

$S$-parameters of the DUT, as shown in Fig. 2(e), were obtained with a Keysight N5247B PNA-X. The measured $S_{11}$ and $S_{22}$ were below −10 and −18 dB from 4 to 8 GHz, respectively, which meant good input and output matching. The measured $S$-parameters were used to calculate the Rollett stability factors [32] plotted in Fig. 2(f). The $K$-factor was larger than 1 and the $|\Delta|$ was smaller than 1 from 0.1 to 45 GHz, which confirmed the unconditional stability of the DUT.

A drawback when modifying the low-pass filter on the gate bias for faster transient operation is reduced suppression of supply fluctuations, which could lead to decreased gain stability over time. The fluctuation of gain over time for both the modified LNA and the commercial LNF-LNC4-8C was measured for 30 s with Keysight P5008A VNA using 6-GHz CW signal under −74-dBm input power and 50-Hz IF bandwidth, as illustrated in Fig. 2(g). The modified LNA demonstrated higher gain fluctuation over time compared with the LNA with an unmodified low-pass filter. While both LNAs exhibit gain fluctuations in the same order of magnitude, the modified LNA shows a fivefold increase in fluctuation, with SDs of 0.020 and 0.004 dB, respectively. The tradeoff between faster transient operation and increased gain fluctuation is inevitable. However, this effect can be mitigated through careful supply regulation and adjustments to the gate bias circuitry in future design iterations.

In summary, the modifications of the HEMT LNA for the faster transient operation had a minor impact on RF performance, as indicated by the static gain and noise,

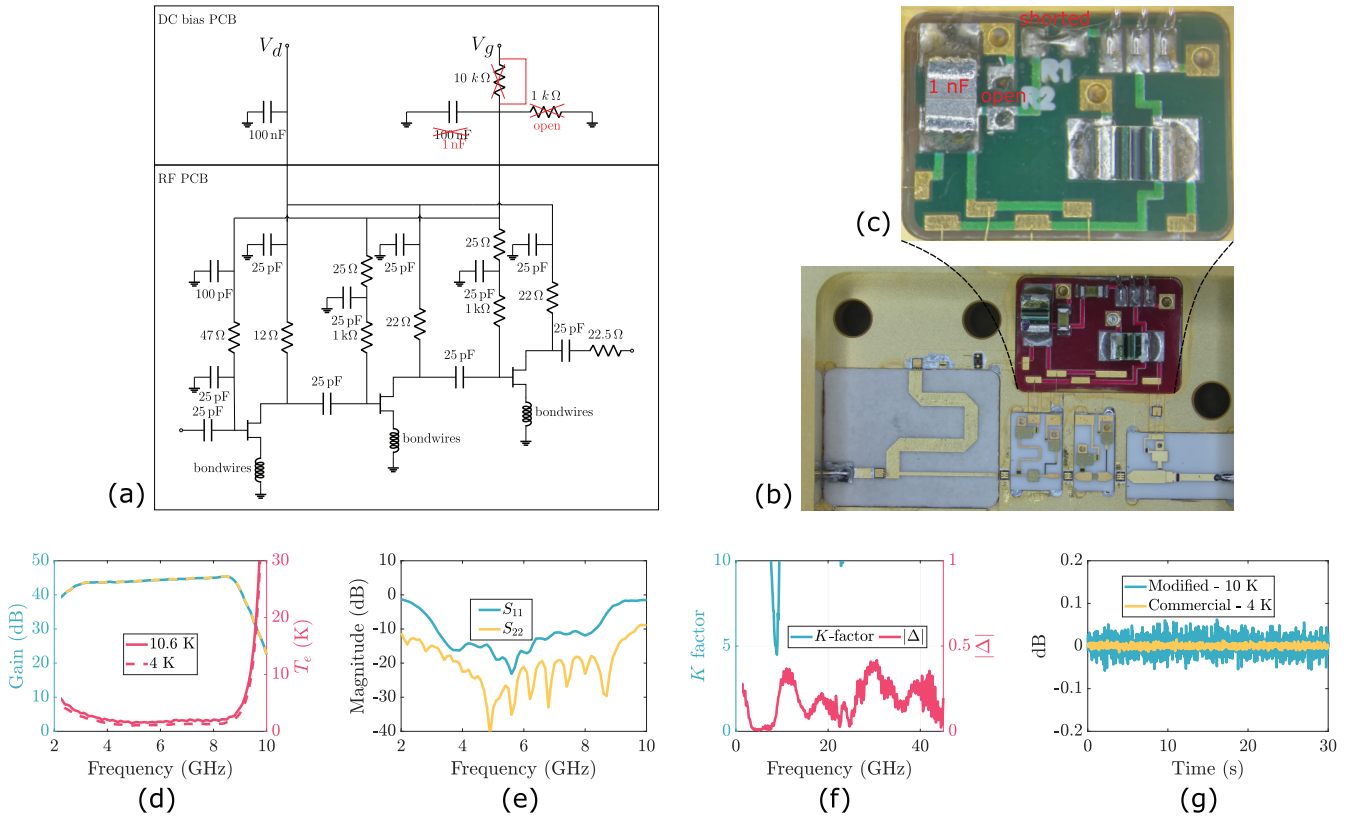


Fig. 2. (a) Bias schematic of the HEMT LNA DUT before and after modification, illustrating the dc and RF PCBs. (b) Image of the DUT circuit before modification. (c) Closed-up view of the modified dc PCB. (d) Static noise and gain characterization of the DUT at 4 and 10.6 K. (e) Measured $S$-parameters at 10.6 K. (f) Rollett stability factors based on measured $S$-parameters. (g) Gain fluctuation comparison over 30 s for the modified LNA and a commercial LNF-LNC4-8C.

$S$-parameters, unconditional stability check, and gain fluctuation measurements.

## III. Cryogenic Time-Domain Noise and Gain Measurement: Set-Up and Verification

Pulsed operation of the HEMT LNA for qubit readout requires the LNA to recover its performance to below 2-K noise temperature with a submicrosecond recovery speed. Characterizing such a rapid recovery in noise is crucial to enable effective pulse operation in qubit readout. To conduct a meaningful analysis, the time resolution should be on the nanosecond scale with noise SD below 1 K. However, to the best of the authors' knowledge, the transient noise behavior of cryogenic LNAs has not yet been characterized.

Based on our previous work on time-domain noise measurement methodology [33], [34], we developed a cryogenic time-domain noise and gain measurement technique to achieve the necessary nanosecond-level time resolution combined with high-noise accuracy. In this approach, an oscilloscope records the output noise signal of the DUT in both "hot" and "cold" states of the noise source. The sampled signal is divided into time intervals defined by the desired time resolution. The power spectral density (PSD) for each interval is calculated using a discrete Fourier transform (DFT). By averaging the PSD within the targeted frequency band and applying the $Y$-factor method, we extract the time-domain equivalent noise temperature and gain of the DUT. A photograph of the measurement setup including a schematic with calibration data is shown in Fig. 3.

The setup contains room temperature (RT) and cryogenic environments. Following a 20-dB cryogenic attenuator, the DUT was placed inside the cryogenic environment maintained at 10.6 K. Semirigid cables were used to connect the input of the attenuator and the output of the DUT to the RT environment. In the RT environment, a Keysight 33500B arbitrary waveform generator (AWG) was used to provide the dc or pulsed gate voltage bias $V_G$. A Keysight 2902A precision source/measure unit (SMU) served as a power supply for the drain voltage bias $V_D$. An HP346B noise source, biased by the same power supply, was connected at the input of the cryogenic DUT system. The output of the DUT was recorded by a Keysight UXR0334A oscilloscope with a maximum of 1.56-ms memory depth when operated at 128-GSa/s sampling speed with 33-GHz bandwidth, followed by an SMA cable and a 3.1–8.4-GHz BPF. A Hall-effect Rohde & Schwarz RT-ZC31 current probe with dc-to-120-MHz bandwidth, connected to the oscilloscope, monitored the transient in $I_D$. A computer was used to enable automatic measurements through instrument control of the power supply, the AWG, and the oscilloscope.

The measurement system can be calibrated using the standard cryogenic attenuator noise measurement method [35], as shown in Fig. 3(b). Excess noise ratio (ENR) of the noise source at RT was provided as a table per frequency by the manufacturer, around 15 dB for the targeted frequency

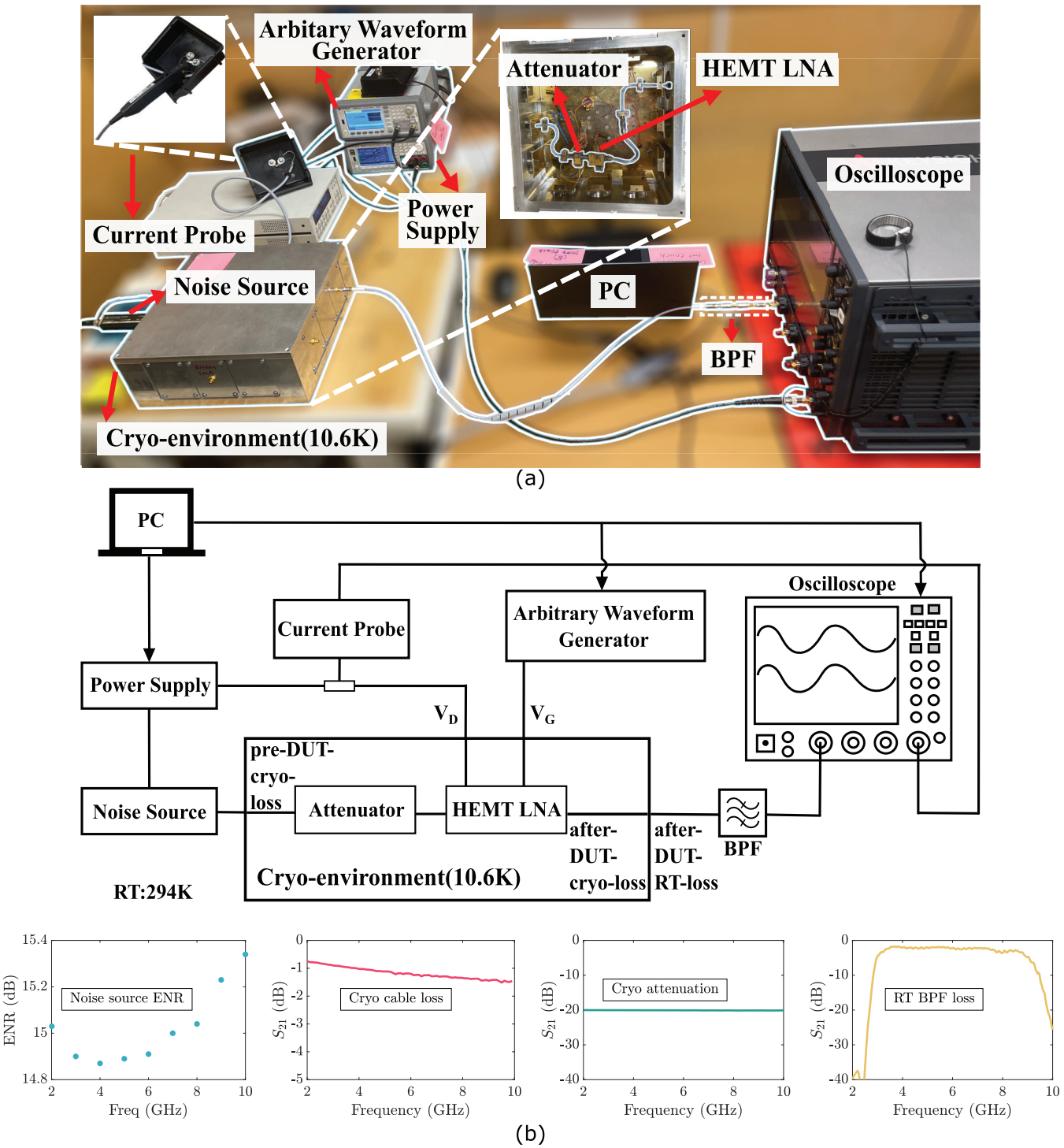


Fig. 3. (a) Cryogenic time-domain noise and gain measurement setup for the HEMT LNA. The setup includes the noise source, current probe, AWG, power supply, bandpass filter (BPF), and oscilloscope. The HEMT LNA and cryogenic attenuator are placed within a cryogenic environment maintained at 10.6 K. A PC is used to control the AWG, the power supply, and the oscilloscope for automated measurements. The closed-up image shows the positioning of the HEMT LNA and attenuator inside the cryo-environment. (b) Schematic of the measurement system, detailing the signal flow from the noise source through the cryo-environment to the oscilloscope. Calibration plots for the noise source ENR, cryogenic cable loss, cryogenic attenuator, and room-temperature BPF loss across the frequency range are presented.

range. The losses of the semirigid cables before the cryogenic attenuator and after the DUT were assumed to be symmetric. The total loss for the cryogenic cables was acquired by connecting them in the cryogenic environment and measuring $S_{21}$ using a PNA-X, resulting in −1.28 dB at 6 GHz. While the input and output cables were not identical, sensitivity tests indicated that a ±0.1 dB variation in input cable loss would lead to an estimated ±0.3 K noise temperature variation at 6 GHz, which is an acceptable margin. The input cable temperature was assumed to be 200 K, and the attenuator temperature, measured using an embedded sensor, was found to be 10.6 K. The cryogenic attenuator was characterized by

TABLE I

VERIFICATION OF CRYOGENIC TIME-DOMAIN NOISE AND GAIN MEASUREMENT SETUP (AVERAGED OVER 3000 REPETITIONS) AVG-T: AVERAGED TIME DOMAIN; SD: STANDARD DEVIATION; AND NS: NOISE SIGNAL

| Freq (GHz) | Time-Domain Measurement | | | Static Measurement | | NS $T_e$ SD (K) |
|---|---|---|---|---|---|---|
| | Avg-T $T_e$ (K) | Avg-T Gain (dB) | $T_e$ SD (K) | NFA $T_e$ (K) | NFA Gain (dB) | |
| 3.0 | 3.08 | 43.54 | 0.35 | 3.17 | 43.15 | 0.0636 |
| 4.0 | 2.00 | 44.54 | 0.29 | 2.05 | 43.77 | 0.0609 |
| 5.0 | 1.69 | 44.53 | 0.23 | 1.52 | 43.95 | 0.0595 |
| 6.0 | 1.72 | 44.76 | 0.24 | 1.71 | 44.39 | 0.0600 |
| 7.0 | 1.85 | 45.02 | 0.26 | 1.81 | 44.65 | 0.0601 |
| 8.0 | 1.85 | 45.94 | 0.24 | 2.07 | 45.01 | 0.0608 |
| 9.0 | 3.40 | 43.69 | 0.37 | 4.16 | 41.56 | 0.0660 |

a similar PNA-X setup by connecting the semirigid cables, showing a flat 20-dB loss across the band. The loss of the external RT SMA cable and the BPF were characterized for compensating the extracted gain using the *Y*-factor method. Ambient temperature in RT and cryogenic environment were measured through resistance thermometers, one measuring the RT and one mounted to the cryogenic attenuator monitored by a Lakeshore 332 temperature controller.

Measured data generated by the calibrated setup were verified by comparing the time-domain noise and gain performance to reference results obtained by the NFA when the DUT was under static dc bias [34]. The time resolution of the measurement was selected to 5 ns based on a tradeoff between computational efficiency and measurement accuracy [34]. The average frequency band was 1 GHz, spanning from 3 to 9 GHz in 1-GHz steps. The 3000 groups of repeated measurements were used for averaging in order to reduce the measured noise variance. The measured time-domain gain and noise under static bias are shown in Fig. 4(a). Despite the fluctuations over the measured period, the gain and noise remain stable for each frequency. The averaged time-domain gain and noise over time are summarized in Table I and plotted together with the NFA measured reference in the frequency domain, see Fig. 4(b). The mean values for time-domain gain and noise acquired by the calibrated cryogenic time-domain gain and noise measurement system from 3 to 8 GHz agree well with the NFA-measured reference data thus verifying the accuracy of the time-domain measurement. The 9-GHz data point is slightly off the reference value, mostly due to frequency averaging at the steep slope of the DUT band edge for both gain and noise performance, as presented in Fig. 2(d).

The fluctuations observed in the measured time-domain noise can be quantified by extracting the SD over time for each frequency, see summary in Table I. For the in-band frequencies from 4 to 8 GHz, measured noise SDs ($T_e$ SD) are below 0.3 K. The measured noise SD for band-edge frequencies at 3 and 9 GHz are slightly higher, likely due to the HEMT's increased matching sensitivity to bias condition fluctuations at the band edges where noise resistance is higher. The theoretical noise SD caused by the noise signal after averaging (NS $T_e$ SD) can be calculated using the noise source ENR, calibrated loss, averaging parameters, and NFA measured noise and gain of DUT via equations in [34]. The NS $T_e$ SD numbers in Table I are smaller than the $T_e$ SD, pointing to additional fluctuations captured by the time-domain noise characterization method. These could include residual fluctuations in the bias voltage, oscilloscope stability, and small variations in the thermal stability of the cryogenic environment.

In this section, we described a cryogenic time-domain gain and noise measurement setup tailored for high-precision characterization of the HEMT LNA under pulsed operation. The system achieves nanosecond-level time resolution and consistent accuracy, as verified against reference measurements under static bias. Noise fluctuations below 0.3-K enable precise observation of the DUT's transient noise response under pulsed conditions.

## IV. TRANSIENT NOISE AND GAIN UNDER SQUARE-WAVEFORM PULSE

The transient noise and gain performance of the HEMT LNA were investigated using square waveform $V_G$ pulses to evaluate its recovery behavior. The pulsewidth of $V_G$ was set to 500 ns, with a pulse period of 5 $\mu$s. In OFF-state, the DUT was biased below the threshold voltage at 100 mV, then switched on to 243 mV, corresponding to a $I_D$ of 15 mA under static bias conditions, with $V_D$ fixed by the power supply in voltage source mode. The rising time of the square waveform produced by the AWG including transmission delay was 15 ns. This delay was negligible compared with the pulsewidth and the DUT's recovery time.

Fig. 5 shows the first 1 $\mu$s of the $V_G$ waveform along with the corresponding output voltage recorded by the oscilloscope and the averaged output power $P_{\text{out}}$ of the DUT for "cold" and "hot" noise source inputs. The $P_{\text{out}}$ values were calculated by averaging the DUT's output voltage over 3000 repetitions. For both noise source inputs, $P_{\text{out}}$ begins to rise sharply above the oscilloscope noise floor around 130 ns after the switch-on of $V_G$. The recovery slope gradually becomes less steep and eventually reaches a steady state around 250 ns. This recovery pattern aligns approximately with the expected behavior of a low-pass filter transfer function. When $V_G$ switches off, $P_{\text{out}}$ drops from the −40 dBm steady state to the noise floor within 10 ns. A small peak appears after the switch-off lasting until 550 ns, likely caused by ringing due to parasitic components in the AWG and power supply.

$P_{\text{out}}$ is a rough estimation for the recovery without frequency resolution. Utilizing the transient gain and noise measurement methodology described in Section III, gain and noise transients, both with 5-ns time resolution and 1-GHz frequency resolution can be acquired to provide a more detailed analysis of the recovery dynamics. A 3-D plot of the transient gain for the DUT using a square-waveform $V_G$ bias is presented in Fig. 6(a) as

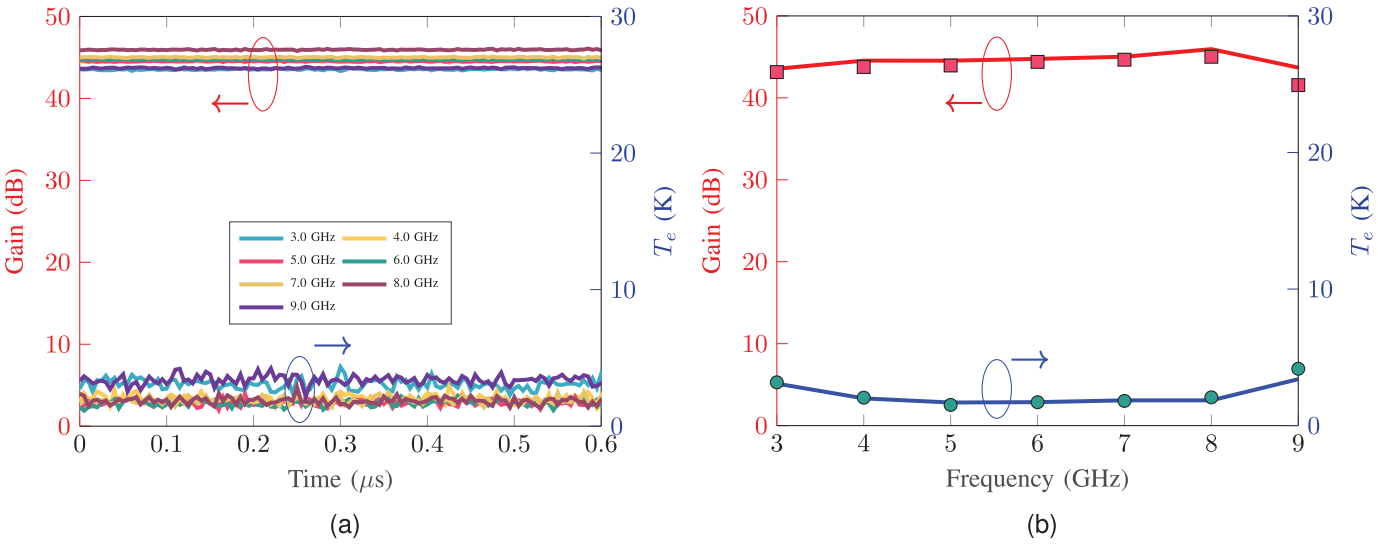


Fig. 4. Time-domain noise and gain of the LNA under dc bias at 10.6 K. (a) Noise and gain for each frequency over time. (b) Mean value of time-domain noise (blue solid line) and gain (red solid line) for each frequency over time compared with noise (blue dot) and gain (red square) obtained by NFA for each frequency.

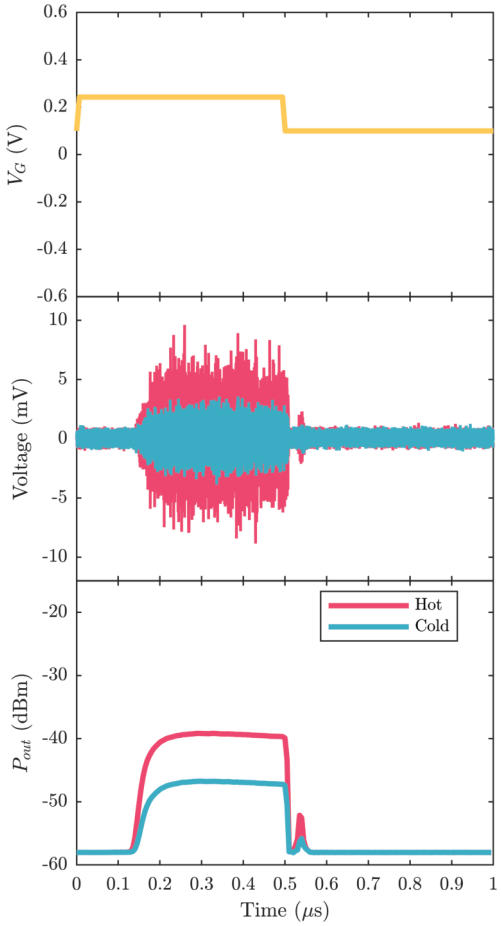


Fig. 5. Square-waveform $V_G$ pulse (top). Time-domain LNA output signal waveform for the noise source in the "hot" and "cold" states (middle). Averaged transient $P_{\text{out}}$ response corresponding to the $V_G$ waveform for the noise source in the "hot" and "cold" states (bottom).

a function of time and frequency. In Fig. 6(b) and (c), the time-domain projection for frequencies from 3 to 9 GHz, in steps of 1 GHz, and the frequency-domain projection for each time step from 0.125 to 0.250 $\mu$s, in steps of 5 ns, are shown. In the time domain, as indicated from the $P_{\text{out}}$ recovery, the transient gain for each frequency is detectable after 130 ns and recovers to its steady performance at around 250 ns. When $V_G$ switches off, the DUT gain drops rapidly below 10 within 10 ns. The peak in $P_{\text{out}}$ results in a gain peak after switching off until 550 ns. The rising edge gain transient projected to the frequency domain shows that the recovery of DUT's gain for each frequency is uniform.

Fig. 7(a) presents the 3-D plot of the transient noise of the DUT under square-waveform $V_G$ bias, with corresponding time-domain and frequency-domain projections shown in Fig. 7(b) and (c), respectively. From the time-domain projection, we observe that the transient noise of the DUT for each frequency drops below 50 K approximately 140 ns after $V_G$ is switched on. The noise level at in-band frequencies attains stable values below 2.0 K after 200 ns. In the frequency-domain projection, the noise transient at in-band frequencies displays a faster recovery rate compared with the band-edge frequencies. This suggests that the noise bandwidth is narrower at the beginning of the DUT's recovery, likely due to a combination of poor matching conditions at the band edges in the circuit design and a relatively high-noise resistance of the HEMT at low-power bias [19].

The recovery pattern of the HEMT LNA under square-waveform $V_G$ pulse is revealed by Figs. 6 and 7. The initial 130 ns delay after switch-on is attributed to the low $I_D$ associated with the low gain at subthreshold bias, effectively keeping the HEMT LNA in a low-power, OFF-state during this period. The actual recovery time (defined as the period when transient gain and noise become detectable and stabilized) is 120 ns, following this delay. Time-domain analysis shows that gain recovers between 130 and 250 ns, whereas noise stabilizes slightly faster, reaching steady state within 200 ns with a noise fluctuation below 0.3 K. In the frequency-domain analysis,

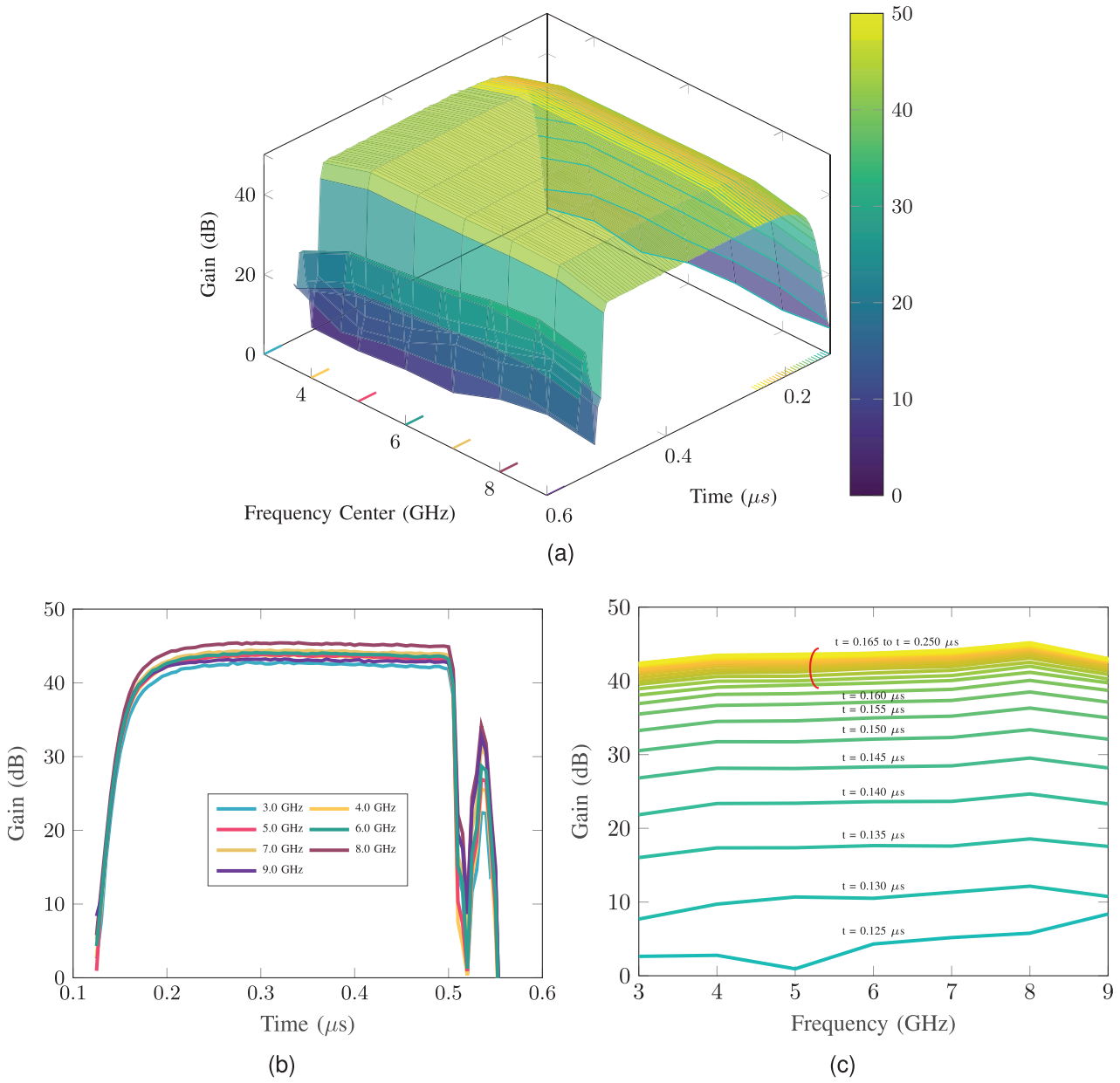


Fig. 6. Time-domain gain of LNA under square waveform $V_G$ bias. (a) 3-D surface plot. (b) Transient gain for each frequency projected to the time domain. (c) Transient gain at each time projected to the frequency domain.

gain recovery is uniform for all frequencies. However noise has slower recovery at the frequency band edges. Overall, the HEMT LNA achieves a 120-ns effective recovery time with a 130-ns delay.

## V. Optimized Pulse Waveform for Fast Recovery

As quantum computing progresses toward faster readout and reset times [24], [36], the demand for rapid recovery of the HEMT LNA becomes increasingly important for efficient pulse operation. In this section, we start with analyzing the factors limiting the recovery speed of the HEMT LNA and explore alternative biasing strategies to improve recovery times. A real-time optimization setup utilizing a GA is developed to search for an optimal bias pulse waveform for fast recovery. Finally, we characterize the HEMT LNA's recovery performance under the optimized pulse waveform and measure the average power consumption.

### A. Recovery Time Analysis

The primary limiting factor for the recovery time of the HEMT LNA is not the intrinsic delay of the InP HEMT itself. The InP HEMT, with parasitic capacitance at the femtofarad level [19], has an intrinsic transient response time below a picosecond [21]. In comparison, the decoupling capacitance in the gate bias of the DUT is 1 nF, as shown in Fig. 2(a), with an experimentally confirmed recovery time exceeding 200 ns in Section IV. Since the HEMT has a much shorter time constant compared with the gate bias low-pass filter, it can be approximated as an instant current source reacting to the voltage applied on its gate electrode $V_{\text{gi}}$. Hence the dominant limiting factor is the low-pass filter in the gate bias

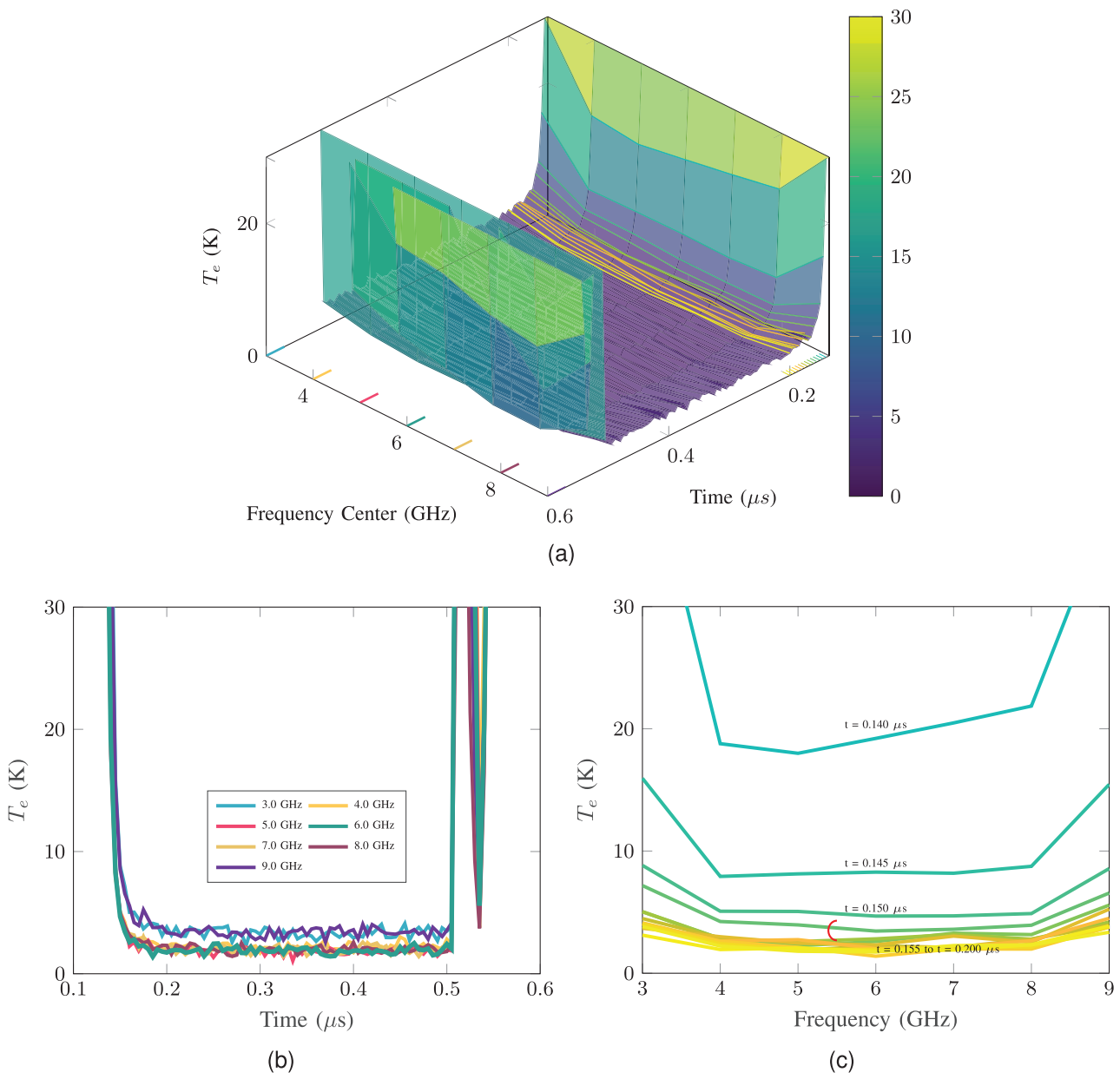


Fig. 7. Time-domain noise of LNA under square waveform $V_G$ bias. (a) 3-D surface plot. (b) Transient noise for each frequency is projected to the time domain. (c) Transient noise at each time is projected to the frequency domain.

line, which includes the parallel capacitance shown in Fig. 2(a) and the output resistance of the AWG after removing the series resistor on the HEMT LNA's dc bias PCB. In addition, the low-pass filter stabilizes the bias conditions and suppresses fluctuations so it cannot be completely removed, as shown in Fig. 2(g).

For an ideal low-pass filter with a parallel capacitance $C$ and series resistance $R$, illustrated in Fig. 8(a), the output response of the $V_{\text{gi}}$ on the HEMT to input $V_G$ applied by the AWG output port can be modeled in the time domain. Assuming that the $V_G$ switch-on acts as a step function, the $V_{\text{gi}}$ recovery can be expressed by

$$V_{\text{gi}}(t) = V_q + \left(V_f - V_q\right)\left(1 - e^{-t/\tau}\right) \tag{1}$$

where $V_f$ is the final voltage, $V_q$ is the initial quiescent voltage, and $\tau = \text{RC}$ is the time constant of the low-pass filter.

Fig. 8(b) illustrates the $V_{\text{gi}}$ response over time for different $V_f$ and $V_q$ bias levels. Since the RF performance does not linearly depend on $V_{\text{gi}}$ and has a threshold voltage determined by the HEMT's large-signal response, combined with the oscilloscope's noise floor, there exists a detectable threshold voltage for $V_{\text{gi}}$, represented as $V_a/2$ in Fig. 8(b). The recovery phase during which $V_{\text{gi}}$ remains below the detectable threshold is the delay period where no recovery curve is observed above the oscilloscope noise floor. For the target voltage $V_t$ assumed to be $V_a$, we define recovery to 99% of $V_t$ when approaching steady state, see Fig. 8(b). The time between $V_{\text{gi}}$ reaching the detectable threshold and reaching 99% of $V_t$ is thus defined as the recovery time. Notably from (1), the slope of $V_{\text{gi}}$ recovery gradually decreases as $t$ increases, aligning with the experimental observations in Section IV. This recovery pattern of the low-pass filter also explains the rapid turn-off transient,

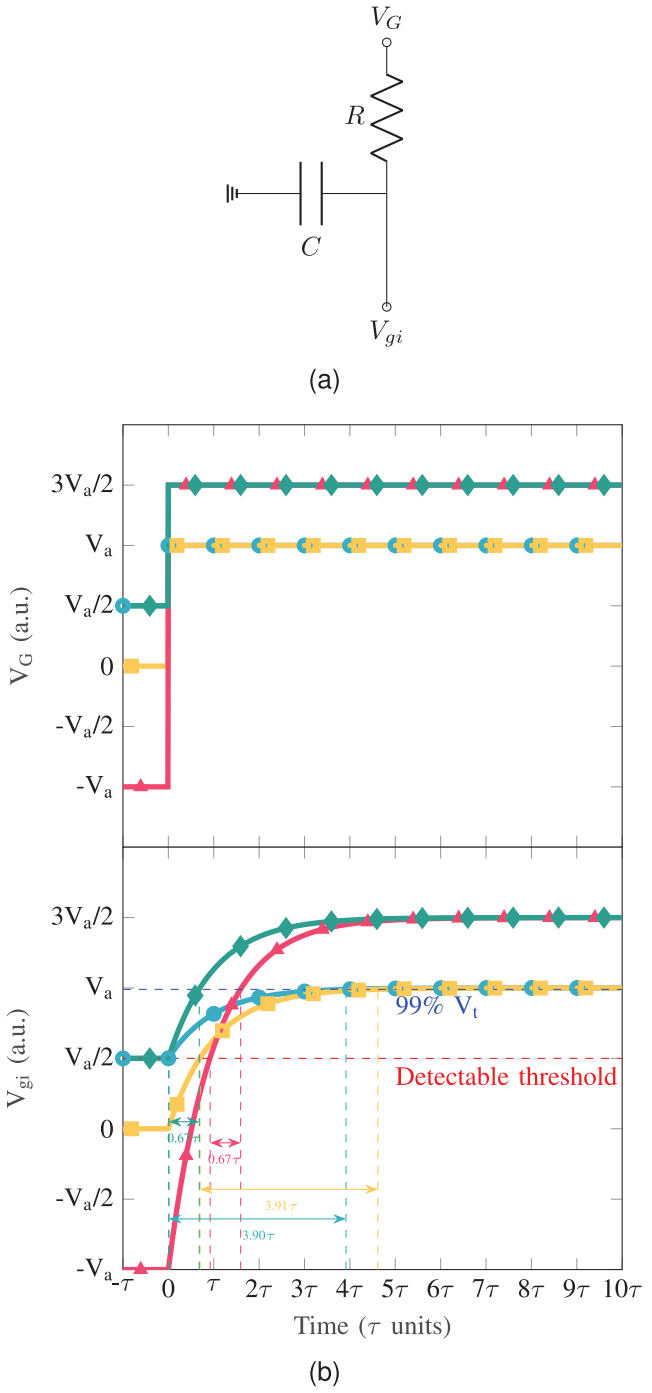


Fig. 8. (a) Ideal *RC* low-pass filter bias circuit. (b) Ideal response of low-pass filter with different quiescent bias and final bias. The top plot shows step function input $V_G$ with different quiescent bias levels. The red triangle line represents a transition from $-V_a$ to $3V_a/2$, the yellow square line from 0 to $V_a$, the blue circle line from $V_a/2$ to $V_a$, and the green diamond line from $V_a/2$ to $3V_a/2$. The bottom plot illustrates the corresponding filtered response $V_{\text{gi}}$.

where the initial fast decay quickly drops $V_{\text{gi}}$ below the HEMT threshold voltage, with less effect from the low-pass filter's slow final recovery phase.

The $V_{\text{gi}}$ response to the step function $V_G$ with different $V_q$ and $V_f$ levels is shown in Fig. 8(b). The switch-on situations between the green diamond line to the red triangle line and the blue circle line to the yellow square line demonstrates

**Algorithm 1** GA for $V_G$ Waveform Optimization

**1. Reference Setup:**
Measure noise floor and desired power level at static bias.
Define the ideal step response $P_{\text{ideal}}(t)$ (noise floor → desired level).
**2. Initialization:**
Define gene vector:

$$X = [v_1, \ldots, v_n, t_1, \ldots, t_{n-1}],$$

where $v_i$ are voltage levels and $t_j$ are time durations.
Set GA parameters (population size, bounds, etc.).
**3. GA Optimization:**
**while** generation $< N_{\text{max\_gen}}$ **do**
  **for** each individual $x$ **do**
    Build $V_G$ waveform in AWG from $x$.
    Measure LNA output by oscilloscope for $P_{\text{out}}(t)$.
    Compute fitness:

$$\text{fitness}(x) = W_1 \cdot \text{rise\_time} + W_2 \cdot \text{mean\_error} + W_3 \cdot \text{max\_error}$$

    where errors are relative to the $P_{\text{ideal}}(t)$.
  **end for**
  Update population via selection, crossover, and mutation (with elitism).
**end while**
**4. Output:** Return the optimal solution:

$$x^* = \arg\min_x \text{fitness}(x), \quad P_{\text{out}}(t) \text{ at } x^*$$

that with the same $V_f$, the deeper quiescent $V_q$ will only lead to longer delay before $V_{\text{gi}}$ reaches the detectable threshold without affecting the recovery time from the threshold to 99% of $V_t$. The switch-on situations between the green diamond line to the blue circle line shows that by initially setting $V_f$ to a higher voltage, such as $3V_a/2$, the recovery time to reach 99% $V_t$ can be significantly shortened, from 3.9 to $0.67\tau$ in this case. This suggests a fast recovery bias strategy to reach target bias by using a higher initial bias to speed up recovery followed by a dynamic adjustment to return to the target $V_t$.

### *B. GA Optimization*

While an ideal low-pass filter analysis suggests that control theory could be used to precompensate the transfer function of the HEMT LNA recovery response with $V_G(t)$ as input, practical limitations can make an analytical solution for the optimal recovery $V_G$ waveform challenging. First, the necessary accurate extraction of the cryogenic large-signal noise model for the HEMT is difficult and not straightforward. Second, changing to different AWG or power supply models introduces variability in output impedance and internal current regulation, which are often not revealed by manufacturers and may significantly alter the transfer function. Third, the large-bypass capacitor, necessary to stabilize the bias, often suffers from high-tolerance deviations [37], which complicates precise analytical modeling. Finally, the influence of parasitic com-

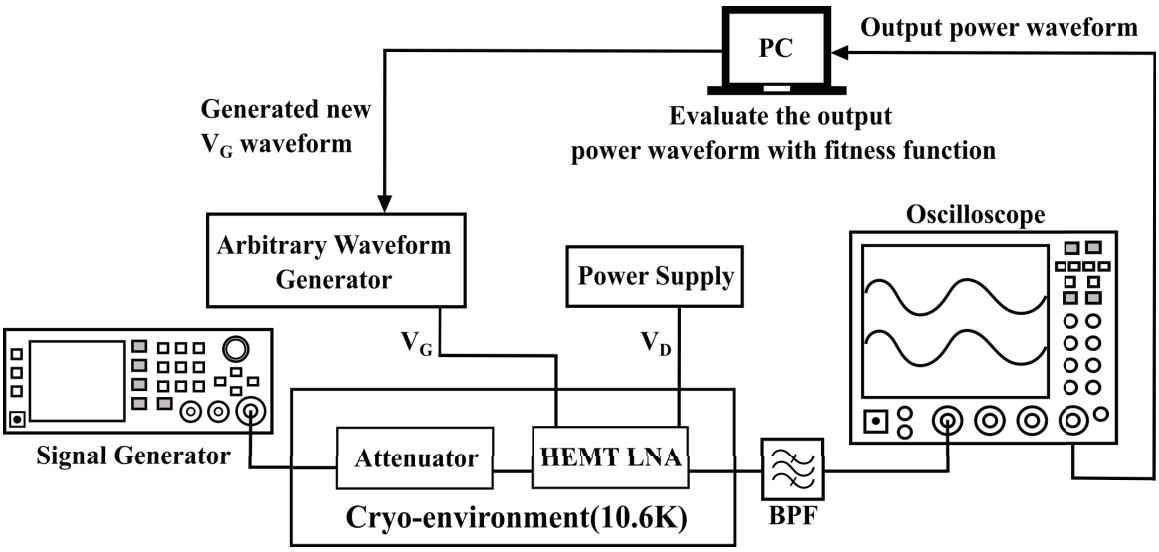


Fig. 9. Setup schematic of real-time GA optimization based on an oscilloscope, AWG, and a signal generator.

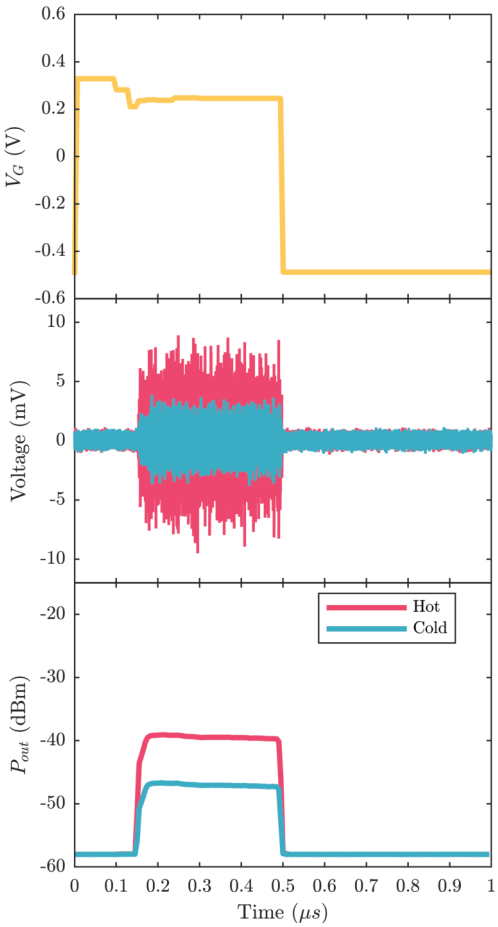


Fig. 10. Optimized fast recovery $V_G$ pulse (top). Time-domain LNA output signal waveform for the noise source in the "hot" and "cold" states (middle). Averaged transient $P_{\text{out}}$ response corresponding to the $V_G$ waveform for the noise source in the "hot" and "cold" states (bottom).

ponents, such as capacitances and resistances on PCBs, adds further complexity that is impractical to quantify accurately.

Due to these challenges, analytical methods are difficult to implement effectively. Instead, a nonlinear optimization approach offers a more robust solution by adapting to uncertainties and complexities without relying on detailed component modeling. In this work, we apply GA to search for a fast recovery bias waveform, primarily to validate the effectiveness of the fast recovery bias strategy. While GA was chosen for its accessibility, other optimization algorithms could be used in future work to further refine and improve recovery performance.

The GA described in Algorithm 1 was implemented in a real-time measurement setup to search for an optimal recovery bias waveform, as shown in Fig. 9. In this setup, the noise source from the cryogenic time-domain noise characterization is replaced by a Keysight 83620B signal generator which injects a −60-dBm CW signal at 6 GHz into the cryogenic system. The PC generates initial populations of $V_G$ waveforms with varying parameters and sends them to the AWG, which pulses the DUT accordingly. The DUT's output voltage is recorded by the oscilloscope and relayed back to the PC to calculate the $P_{\text{out}}$ transient, serving as a preliminary indicator for the HEMT LNA's recovery.

The $P_{\text{out}}$ transient is evaluated in the fitness function based on its recovery time and flatness after recovery. Here, the recovery time is defined specifically for the optimization process as the time taken for $P_{\text{out}}$ to rise from the noise floor to 99% of the target steady-state power, calibrated from the dc bias. The GA then applies genetic selection, using crossover and mutation operations to evolve waveform parameters toward minimizing recovery time and achieving a stable postrecovery state. Each successive generation refines the waveform, progressively enhancing the speed and stability of the DUT's recovery performance.

For efficient GA optimization, the 500-ns waveform pulse is divided into seven stages, each with adjustable duration and voltage amplitude as parameters. Including the quiescent amplitude, there are a total of 15 parameters for optimization. With a population size of 20 per generation and an optimization run of 20 generations, the GA produced the optimized $V_G$ waveform for fast recovery, along with the resulting

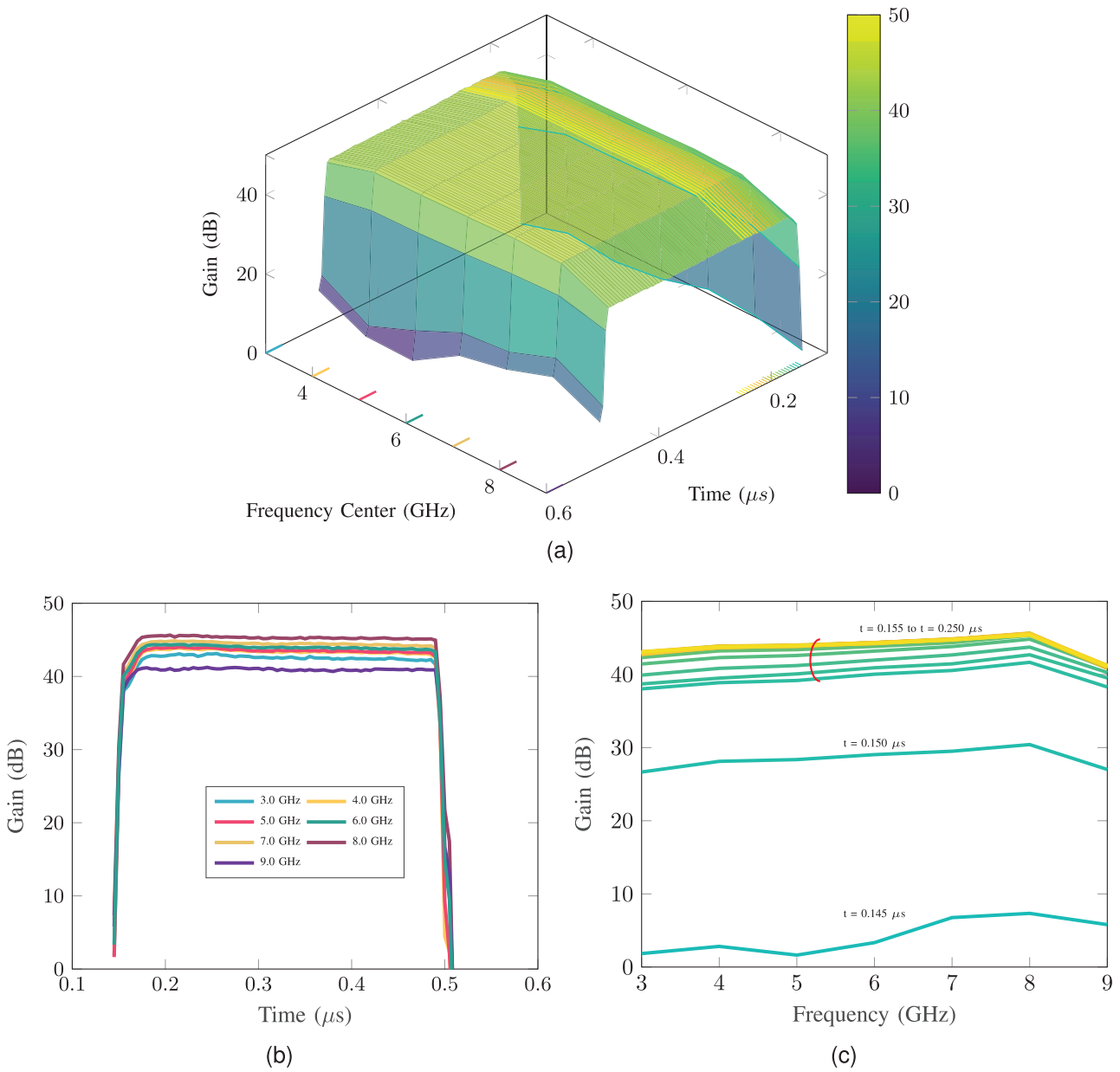


Fig. 11. Time-domain gain of LNA under optimized fast-recovery waveform $V_G$ bias. (a) 3-D surface plot. (b) Transient gain for each frequency projected to the time domain. (c) Transient gain at each time projected to the frequency domain.

time-domain output voltage and $P_{\text{out}}$ transient, as illustrated in Fig. 10.

The optimized $V_G$ waveform features multiple amplitude steps. The initial high step of 94 ns quickly raises $V_{\text{gi}}$ above the threshold voltage, facilitating a rapid transition to the active state. Subsequent steps then progressively lower the gate voltage, maintaining recovery momentum and suppressing the transient peak induced by the initial high-step voltage. The quiescent voltage of −500 mV, well below the HEMT threshold voltage, ensures a fast switch-off with minimal peaks, which might otherwise arise from power supply regulator circuits.

In the resulting $P_{\text{out}}$ transient for both "hot" and "cold" noise source states, recovery begins at 145 ns and reaches a steady state by 180 ns without any overshoot. A gradual decrease of approximately 0.45 dB is observed over the subsequent 300 ns, likely due to the power supply regulator. While this slight slope is suboptimal, it remains within acceptable limits for the current study and does not impact the primary focus on the recovery performance. Future improvements, such as using a more stable power supply or further refining the optimization, could be implemented to enhance flatness at a steady state.

### C. Transient Performance Characterization

The transient gain of the LNA with the optimized fast-recovery $V_G$ waveform is illustrated in Fig. 11. The 3-D plot in Fig. 11(a) illustrates the gain as a function of time and frequency, demonstrating a faster response compared with the square waveform $V_G$ configuration. In the time-domain projection, shown in Fig. 11(b), the gain transient begins to recover after a 145-ns delay, reaching steady state across all

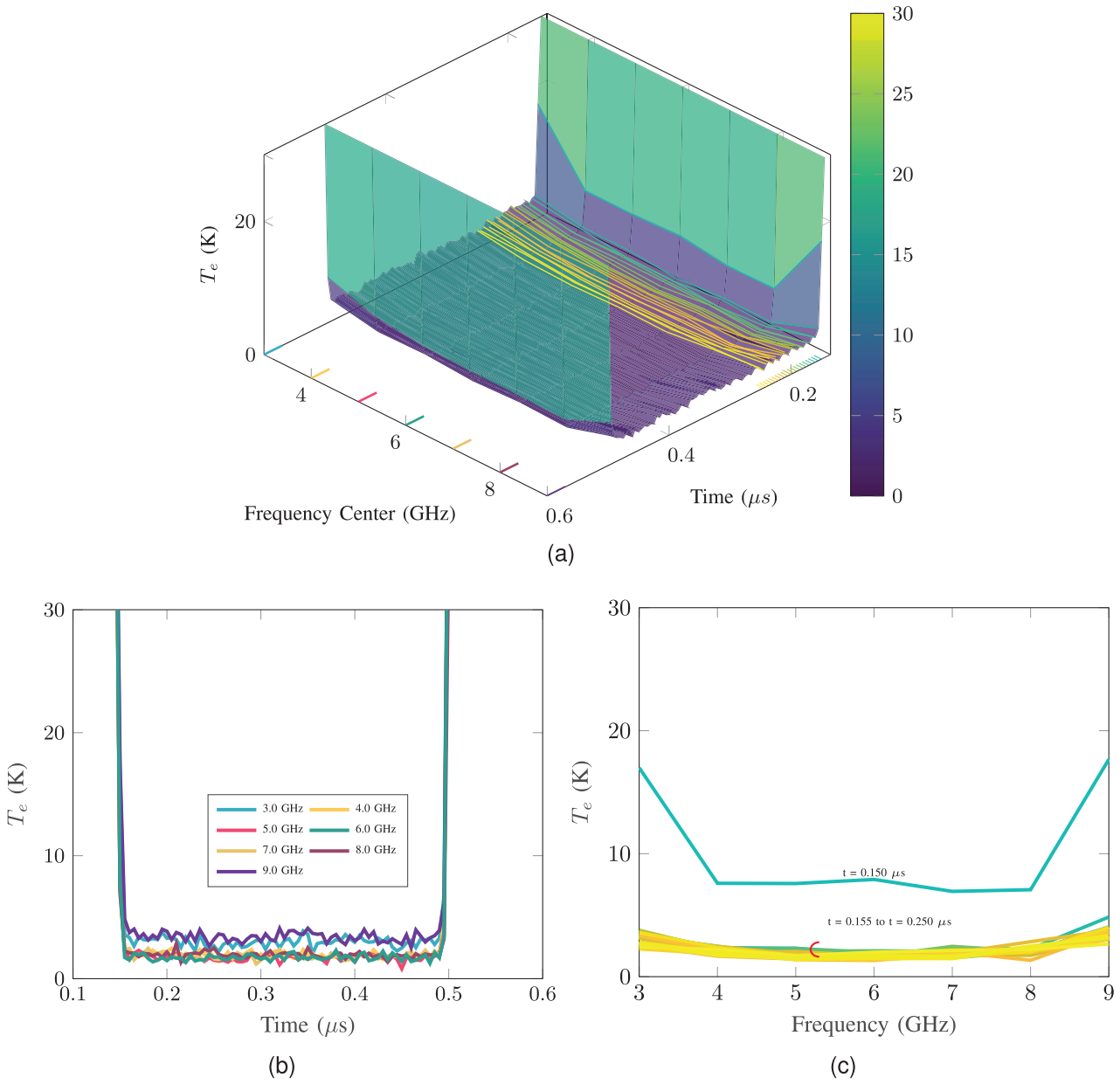


Fig. 12. Time-domain noise of LNA under optimized fast-recovery waveform $V_G$ bias. (a) 3-D surface plot. (b) Transient noise for each frequency is projected to the time domain. (c) Transient noise at each time projected to the frequency domain.

frequencies by 180 ns. Compared with the square-waveform pulse, the optimized waveform achieves gain recovery 85 ns faster although with 15 ns longer delay before recovery begins. Following this steady state, the gain transient shows a gradual 0.5 dB decrease over the next 300 ns, which aligns with the $P_{\text{out}}$ transient under the optimized fast-recovery $V_G$ waveform. When switching off, the gain transient returns to the quiescent state within 20 ns after $V_G$ is switched, with no peaks detected. In the frequency-domain projection, the gain recovery is uniform across frequencies, indicating consistent performance throughout the operational bandwidth.

Fig. 12 shows the transient noise behavior using the optimized waveform. Compared with the gain recovery, the noise recovery is even faster, with effective noise temperature stabilizing below 2 K for in-band frequencies within 20 after 145-ns delay. Unlike the gain transient, no tilting is observed in the noise transient with noise SD below 0.3 K. The turn-off transient is within 10 ns and exhibits no peak. The frequency-domain projection in Fig. 12(c) reveals an initial slower recovery at frequency band edges but a quick return to steady-state across all frequencies. The optimized fast-recover $V_G$ waveform reduces the overall recovery time to around 35 ns, which is one order of magnitude below typical qubit readout times, making it suitable for qubit readout applications.

The HEMT LNA with optimized fast recovery $V_G$ was tested under a realistic scenario for qubit readout pulse-operation, with a 500-ns $V_G$ pulsewidth repeated every 5 $\mu$s. The gain and noise transients in two cycles are presented in Fig. 13. Excluding the initial delay and recovery time, the amplifier maintains 320 ns of stable recovered performance for qubit readout during each cycle. The gain and noise

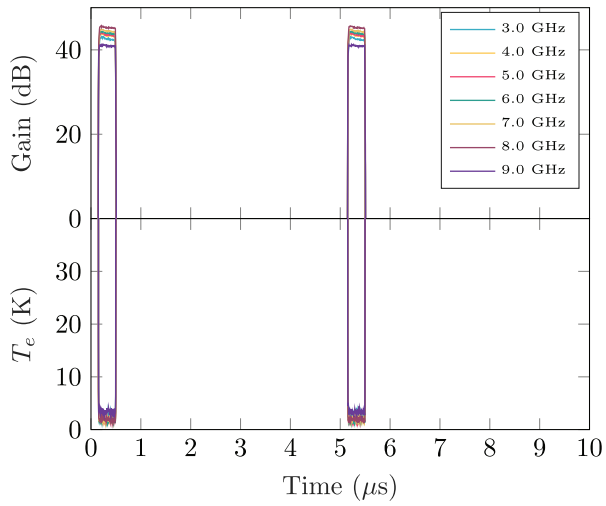


Fig. 13. Gain and noise transient of DUT with optimized fast recovery $V_G$ waveform in two 5-$\mu$s period with 500-ns pulsewidth.

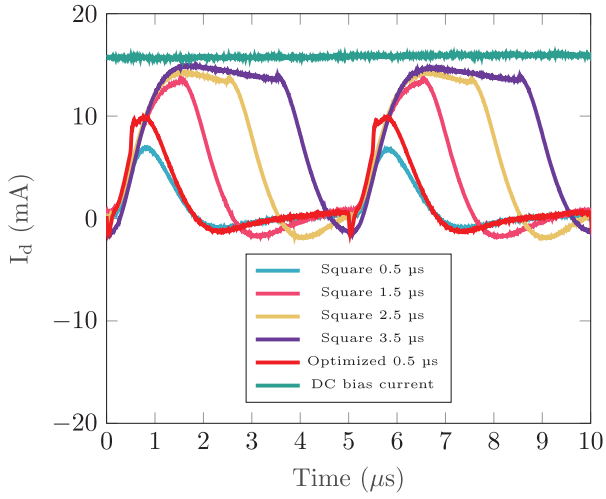


Fig. 14. (a) $I_D$ current transient comparison between $V_G$ of dc bias, square waveform with different pulse widths, and optimized fast recovery waveform. (b) Averaged power consumption percentage compared with static $V_G$ bias for square waveform and optimized fast recovery waveform both with 0.5-$\mu$s pulsewidth and 5-$\mu$s pulse period.

transients remain consistent across cycles, indicating reliable performance between pulses.

The $I_D$ transient under different $V_G$ configurations, including the dc bias, square waveforms of various pulsewidths, and the optimized fast-recovery waveform, are compared in Fig. 14(a). Note that the $I_D$ transient probe was positioned at the power supply port outside the cryogenic environment, as shown in Fig. 3(a). As a result, the recorded $I_D$ transient does not reflect the actual drain current inside the HEMT but rather the current after the 100-nF drain-side capacitor.

When the power supply operates in voltage mode, the HEMT functions as a current source controlled by $V_G$ with a very short delay. Due to the presence of the drain capacitor, the $I_D$ transient shows a much longer charge and discharge time compared with the actual HEMT LNA's transient response. Importantly, this means that the $I_D$ transient, even if it does not drop to zero, does not influence the HEMT LNA's switching state. The HEMT LNA itself can turn on or off swiftly with low time constant, ensuring that no channel power dissipation occurs when the amplifier is switched off, thereby mitigating potential interferences with the qubits.

For $V_G$ square waveforms with pulse widths greater than 1.5 $\mu$s, which allow sufficient charge and discharge time for the drain capacitor, the $I_D$ transient returns to the dc bias amplitude. The slow decrease slope observed before $V_G$ switch-off can be attributed to the internal regulator of the power supply. With shorter pulse widths, the $I_D$ transient shows a reduced peak amplitude due to insufficient charge time. Thanks to the initial high-voltage step in the optimized fast recovery waveform, its $I_D$ transient reaches a higher peak more rapidly compared to a square-waveform pulse with the same pulsewidth of 0.5 $\mu$s.

Although the $I_D$ transient does not reflect the transient performance of the HEMT LNA, it can be used to calculate the average power consumption in the cryogenic system. The average power consumption can be acquired by integrating the $I_D$ transients for one period. The average power consumption per period of 0.5 $\mu$s with 10% duty cycle of the HEMT LNA under square-waveform pulse and optimized fast-recovery waveform is compared to static dc bias in Fig. 14(b). Pulsed operation for both waveform configurations reduces the power consumption approximately to the duty cycle. The optimized fast recovery waveform, however, has a faster recovery time compared with the square waveform pulse at a slightly higher average power consumption of 13.9%.

In summary, the optimized fast-recovery waveform outperforms the square waveform configuration in achieving a recovery time of approximately 35 ns hence meeting the requirement for qubit readout. This improvement in transient response, combined with reduced power dissipation, enables the pulsed operation of the HEMT LNA as a potential solution for qubit readout.

## VI. Conclusion

This work presented pulsed operation of the cryogenic HEMT LNA aimed for qubit readout at very low-dc power in large-scale quantum computing systems. We demonstrated that the LNA power dissipation can be significantly reduced without compromising critical performance by implementing pulsed operation. A modified HEMT LNA for fast recovery

was characterized using a customized cryogenic time-domain noise and gain measurement setup with a time resolution of 5 ns and noise SD below 0.3 K. Analysis of the transient performance revealed distinct recovery behaviors in both time and frequency domains: In the time domain, noise stabilized faster than gain; in the frequency domain, noise recovery showed an initial slower recovery at frequency band edges before converging to a stable state, whereas gain recovery was uniform across all frequencies. Further analysis identified the low-pass filter in the gate bias line as the primary limiting factor for fast recovery. Using a GA, we optimized the gate voltage waveform, achieving a 35-ns recovery time. When tested under a qubit readout scenario with a 500-ns pulsewidth and 5-$\mu$s period, the pulse-operated LNA demonstrated stable, repeatable performance between pulses. The optimized pulse operation showed an average power consumption reduction to 13.9% of static dc bias power consumption, aligning with the duty cycle of the experiment. This study offers a promising path forward for efficient, low-power amplification solutions essential for large-scale quantum readout applications.

## ACKNOWLEDGMENT

The authors would like to express their gratitude to Liangyu Chen, Hangxi Li, Tong Liu, and Xenia Lööv from the Chalmers University of Technology, Göteborg, Sweden, for insightful discussions. They also extend their thanks to Hannes Hanhineva, Johan Embretsen, Sumedh Mahashabde, and David Niepce from Low Noise Factory AB, Göteborg, Sweden, for their assistance with the assembly and measurements of the low-noise amplifiers (LNAs), as well as for their valuable input.

## REFERENCES

[1] Y. Kim et al., "Evidence for the utility of quantum computing before fault tolerance," *Nature*, vol. 618, no. 7965, pp. 500–505, Jun. 2023.

[2] S. Aaronson and L. Chen, "Complexity-theoretic foundations of quantum supremacy experiments," 2016, *arXiv:1612.05903*.

[3] F. Arute et al., "Quantum supremacy using a programmable superconducting processor," *Nature*, vol. 574, no. 7779, pp. 505–510, 2019.

[4] A. Morvan et al., "Phase transitions in random circuit sampling," *Nature*, vol. 634, no. 8033, pp. 328–333, Oct. 2024.

[5] IBM. *IBM Quantum Computer Road Map*. Accessed: Jan. 15, 2023. [Online]. Available: https://www.ibm.com/quantum/roadmap

[6] A. G. Fowler, M. Mariantoni, J. M. Martinis, and A. N. Cleland, "Surface codes: Towards practical large-scale quantum computation," *Phys. Rev. A, Gen. Phys.*, vol. 86, pp. 032324.1–032324.48, Sep. 2012.

[7] Google Quantum AI, "Suppressing quantum errors by scaling a surface code logical qubit," *Nature*, vol. 614, no. 7949, pp. 676–681, Feb. 2023.

[8] R. Acharya et al., "Quantum error correction below the surface code threshold," 2024, *arXiv:2408.13687*.

[9] S. Krinner et al., "Engineering cryogenic setups for 100-qubit scale superconducting circuit systems," *EPJ Quantum Technol.*, vol. 6, no. 1, p. 2, May 2019.

[10] M. Kristen et al., "Amplitude and frequency sensing of microwave fields with a superconducting transmon qudit," *npj Quantum Inf.*, vol. 6, no. 1, p. 57, Jun. 2020.

[11] Y. Lu et al., "Steady-state heat transport and work with a single artificial atom coupled to a waveguide: Emission without external driving," *PRX Quantum*, vol. 3, no. 2, Apr. 2022, Art. no. 020305.

[12] D. Sank et al., "Measurement-induced state transitions in a superconducting qubit: Beyond the rotating wave approximation," *Phys. Rev. Lett.*, vol. 117, no. 19, Nov. 2016, Art. no. 190503.

[13] A. M. Korolev, V. M. Shulga, O. G. Turutanov, and V. I. Shnyrkov, "Measurement of brightness temperature of two-dimensional electron gas in channel of a high electron mobility transistor at ultralow dissipation power," *Solid-State Electron.*, vol. 121, pp. 20–24, Jul. 2016.

[14] M. Malnou et al., "A traveling-wave parametric amplifier and converter," 2024, *arXiv:2406.19476*.

[15] H. Renberg Nilsson, D. Shiri, R. Rehammar, A. Fadavi Roudsari, and P. Delsing, "Peripheral circuits for ideal performance of a traveling-wave parametric amplifier," *Phys. Rev. Appl.*, vol. 21, no. 6, Jun. 2024, Art. no. 064062.

[16] E. I. Rosenthal et al., "Efficient and low-backaction quantum measurement using a chip-scale detector," *Phys. Rev. Lett.*, vol. 126, no. 9, Mar. 2021, Art. no. 090503.

[17] F. Lecocq et al., "Efficient qubit measurement with a nonreciprocal microwave amplifier," *Phys. Rev. Lett.*, vol. 126, no. 2, Jan. 2021, Art. no. 020502.

[18] Y. Zeng, J. Stenarson, P. Sobis, N. Wadefalk, and J. Grahn, "A 100-$\mu$W 4–6 GHz cryogenic InP HEMT LNA achieving an average noise temperature of 2.6 k," in *Proc. Asia–Pacific Microw. Conf. (APMC)*, Nov. 2022, pp. 13–15.

[19] Y. Zeng, J. Stenarson, P. Sobis, N. Wadefalk, and J. Grahn, "Sub-mW cryogenic InP HEMT LNA for qubit readout," *IEEE Trans. Microw. Theory Techn.*, vol. 72, no. 3, pp. 1606–1617, Mar. 2024.

[20] Y. Zeng, J. Li, J. Stenarson, P. Sobis, and J. Grahn, "100-$\mu$W cryogenic HEMT LNAs for quantum computing," in *Proc. 18th Eur. Microw. Integr. Circuits Conf. (EuMIC)*, Sep. 2023, pp. 71–74.

[21] E. Cha et al., "Optimization of channel structures in InP HEMT technology for cryogenic low-noise and low-power operation," *IEEE Trans. Electron Devices*, vol. 70, no. 5, pp. 2431–2436, May 2023.

[22] A. Blais, A. L. Grimsmo, S. M. Girvin, and A. Wallraff, "Circuit quantum electrodynamics," *Rev. Mod. Phys.*, vol. 93, no. 2, May 2021, Art. no. 025005.

[23] Y. Sunada et al., "Fast readout and reset of a superconducting qubit coupled to a resonator with an intrinsic Purcell filter," *Phys. Rev. Appl.*, vol. 17, no. 4, Apr. 2022, Art. no. 044016.

[24] J. Heinsoo et al., "Rapid high-fidelity multiplexed readout of superconducting qubits," *Phys. Rev. Appl.*, vol. 10, no. 3, Sep. 2018, Art. no. 034040.

[25] T. Walter et al., "Rapid high-fidelity single-shot dispersive readout of superconducting qubits," *Phys. Rev. Appl.*, vol. 7, no. 5, May 2017, Art. no. 054020.

[26] L. Chen et al., "Transmon qubit readout fidelity at the threshold for quantum error correction without a quantum-limited amplifier," *npj Quantum Inf.*, vol. 9, no. 1, p. 26, Mar. 2023.

[27] N. Sundaresan et al., "Demonstrating multi-round subsystem quantum error correction using matching and maximum likelihood decoders," *Nature Commun.*, vol. 14, no. 1, p. 2852, May 2023.

[28] Y. Zhao et al., "Realization of an error-correcting surface code with superconducting qubits," *Phys. Rev. Lett.*, vol. 129, no. 3, Jul. 2022, Art. no. 030501.

[29] S. Krinner et al., "Realizing repeated quantum error correction in a distance-three surface code," *Nature*, vol. 605, no. 7911, pp. 669–674, May 2022.

[30] Low Noise Factory,. *LNF4-8C Datasheet*. Accessed: Mar. 22, 2022. [Online]. Available: https://www.lownoisefactory.com/wp-content/uploads/2022/03/lnf-lnc4_8c.pdf

[31] J. L. Cano, N. Wadefalk, and J. D. Gallego-Puyol, "Ultra-wideband chip attenuator for precise noise measurements at cryogenic temperatures," *IEEE Trans. Microw. Theory Techn.*, vol. 58, no. 9, pp. 2504–2510, Sep. 2010.

[32] D. M. Pozar, *Microwave Engineering*. Hoboken, NJ, USA: Wiley, 2011.

[33] Y. Zeng, J. Stenarson, P. Sobis, and J. Grahn, "Transient noise and gain characterization for pulse-operated LNAs," *IEEE Microw. Wireless Technol. Lett.*, vol. 34, no. 7, pp. 911–914, Jul. 2024.

[34] Y. Zeng, J. Stenarson, P. Sobis, and J. Grahn, "Time-domain noise characterization of LNAs: Validation, trade-offs, and analytical insights," in *Proc. ARFTG Microw. Meas. Conf*, Jan. 2025, pp. 1–18.

[35] J. Fernandez, "A noise-temperature measurement system using a cryogenic attenuator," *TMO Prog. Rep.*, vol. 15, pp. 42–135, Nov. 1998.

[36] P. Magnard et al., "Fast and unconditional all-microwave reset of a superconducting qubit," *Phys. Rev. Lett.*, vol. 121, no. 6, Aug. 2018, Art. no. 060502.

[37] KEMET Electron. Corp. *Surface Mount Multilayer Ceramic Chip Capacitors*. Accessed: Feb. 16, 2025. [Online]. Available: https://docs.rs-online.com/e5cd/0900766b81705e7a.pdf

**Yin Zeng** (Graduate Student Member, IEEE) was born in Chongqing, China, in 1996. He received the M.Sc. degree in wireless, photonics, and space engineering from Chalmers University of Technology, Göteborg, Sweden, in 2020, where he is currently pursuing the Ph.D. degree in microwave technology.

His research interests include low-power, low-noise amplifier (LNA) design, cryogenic electronics, transistor characterization and modeling, and transient noise characterization.

**Jörgen Stenarson** (Member, IEEE) received the M.Sc. degree in engineering physics and the Ph.D. degree in microwave electronics from the Chalmers University of Technology, Göteborg, Sweden, in 1997 and 2001, respectively.

In 2002, he joined SP Technical Research Institute, Borås, Sweden, where he worked on microwave metrology with a focus on network analyzers. In 2015, he joined the Department of Microtechnology and Nanoscience, Chalmers University of Technology to manage the creation of the Kollberg Laboratory with a grant from the Wallenberg Foundation. In 2017, he joined Low Noise Factory AB, Göteborg, where he is currently the CTO. His research interests are microwave metrology and low-noise amplifier design.

**Peter Sobis** was born in Göteborg, Sweden, in 1978. He received the M.Sc. degree in electrical engineering and the Licentiate and Doctoral degrees in THz electronics from the Chalmers University of Technology, Göteborg, in 2003, 2010, and 2016, respectively.

From 2003 to 2004, he was with Anaren Microwave Inc., Syracuse, NY, USA, working on passive microwave components and beamforming networks. From 2004 to 2021, he was with Omnisys Instruments AB, Västra Frölunda, Sweden, where he was responsible for the development of radiometer components and subsystems for various ESA missions supported by the Swedish National Space Board projects. In 2018, he became an Adjunct Professor with the Department of Microtechnology and Nanoscience (MC2), Chalmers University of Technology. In 2021, he joined Low Noise Factory AB, Göteborg, specializing in production of cryogenic low-noise amplifiers. His current research involves InP HEMT low-noise amplifiers (LNAs) and THz Schottky-based receivers for quantum computing, Earth observation, and radio astronomy applications.

**Jan Grahn** (Senior Member, IEEE) received the Ph.D. degree in solid-state electronics from the Royal Institute of Technology (KTH), Stockholm, Sweden, in 1993.

He was a Post-Doctoral Researcher with KTH, where he focused on SiGe HBT technology. In 2001, he joined the Chalmers University of Technology, Göteborg, Sweden. His current research interests include narrowbandgap high-electron mobility transistor technology for low-noise and low-dc power dissipation.